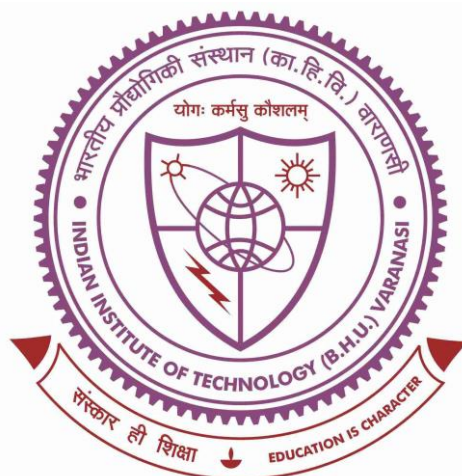


# Drug Repurposing as a Therapeutic Approach to Neuroprotection



**Thesis submitted in partial fulfilment for the  
Award of Degree**

**Doctor of Philosophy**

**By**

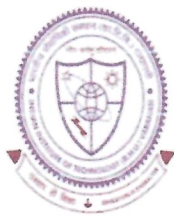
**Anindita Bhattacharjee, M.Pharm.**

**School of Biomedical Engineering  
Indian Institute of Technology  
(Banaras Hindu University)  
Varanasi-221005, India**

**Roll No. 18021003**

**Year: 2023**





**School of Biomedical Engineering  
Indian Institute of Technology  
(Banaras Hindu University)  
Varanasi – 221 005**

---

**CERTIFICATE**

It is certified that the work contained in the thesis titled “**Drug repurposing as a therapeutic approach to Neuroprotection**” by “**Anindita Bhattacharjee**” has been carried out under my supervision and that this work has not been submitted elsewhere for a degree.

It is further certified that the student has fulfilled all the requirements of Comprehensive Examination, Candidacy and SOTA for the award of Ph.D. Degree.

**(Prof. Prasun Kumar Roy)  
Supervisor**

**(Dr. Shiru Sharma)  
Co-Supervisor**

**Date: 27/7/23  
Place: IIT (BHU), Varanasi**





School of Biomedical Engineering  
Indian Institute of Technology  
(Banaras Hindu University)  
Varanasi - 221 005

### DECLARATION BY THE CANDIDATE

I, “Anindita Bhattacharjee”, certify that the work embodied in this Ph.D. thesis is my own bona fide work and carried out by me under the supervision of “Prof. Prasun Kumar Roy” and “Dr. Shiru Sharma” from “July 2018” to “July 2023” at the “School of Biomedical Engineering”, Indian Institute of Technology (IIT), Varanasi. The matter embodied in this thesis has not been submitted for the award of any other degree/diploma. I declare that I have faithfully acknowledged and given credits to the research workers wherever their works have been cited in my work in this thesis. I further declare that I have not willfully copied any other’s work, paragraphs, text, data, results, etc., reported in the journals, books, magazines, reports, dissertations, theses, etc., or available at websites and have not included them in this Ph.D. thesis and have not cited as my own work.

Date: 27/7/23  
Place: IIT (IIT), Varanasi

Anindita Bhattacharjee  
Anindita Bhattacharjee

### CERTIFICATE FROM THE SUPERVISOR

It is certified that the above statement made by the student is correct to the best of our knowledge.

Prasun Roy 27/7/23  
(Prof. Prasun Kumar Roy)  
Supervisor

Dr. Shiru Sharma  
(Dr. Shiru Sharma)  
Co-Supervisor

S. Kumar  
(Coordinator) 27/07/23

School of Biomedical Engineering  
Indian Institute of Technology (IIT)  
Varanasi-221005, India

समन्वयक/CO-ORDINATOR  
जैव चिकित्सा अभियांत्रिकी स्कूल  
SCHOOL OF BIOMEDICAL ENGG.  
भारतीय प्रौद्योगिकी संस्थान (का.हि.वि.)  
INDIAN INSTITUTE OF TECHNOLOGY (I.I.T.)  
वाराणसी 221005/VARANASI-221005





School of Biomedical Engineering  
Indian Institute of Technology  
(Banaras Hindu University)  
Varanasi - 221 005

---

## COPYRIGHT TRANSFER CERTIFICATE

**Title of the Thesis:** “Drug repurposing as a therapeutic approach to Neuroprotection”

**Name of the Student:** Anindita Bhattacharjee

### Copyright Transfer

The undersigned hereby assigns to the Indian Institute of Technology (Banaras Hindu University), Varanasi all rights under copyright that may exist in and for the above thesis submitted for the award of the “**Doctor of Philosophy**”

**Date:** 27/7/23  
**Place:** Varanasi

Anindita Bhattacharjee  
Anindita Bhattacharjee

**Note:** However, the author may reproduce or authorize others to reproduce material extracted verbatim from the thesis or derivative of the thesis for author’s personal use provided that the source and University’s copyright notice are indicated.



## **Acknowledgment**

It is my privilege to express my gratitude to the founder of Banaras Hindu University, Bharat Ratna Pandit Madan Mohan Malaviya Ji, who made this glorious place as capital of education. The five years of hard work have finally come to an end. My chosen specialization is a relatively new area of Medical Neuroscience, bringing tools and validation from the various Physical science, Engineering, and Life sciences to help in the conception of better therapy paradigms. I am thankful to Prof. Prasun Kumar Roy, for allowing me to complete my PhD under his supervision and for exposing me to this fascinating area of research. I would also like to thank my co-supervisor Dr. Shiru Sharma for her expert opinions and guidance throughout the duration of my PhD. They have always been a source of encouragement as well as a patient bearer of my faults. I feel really honored, and it has been a true pleasure for me to serve under them.

My sincere appreciation goes to Dr. Alexandre Routier of the Aramis lab for assisting me in comprehending the newly developed PET image analysis platform, Clinica. I would also like to thank the ExploreASL platform development team, led by Dr. Jan Petr, Ms. Esteves Padrela, and Mr. Michael Stritt for helping me to understand the ASL image processing. I would like to thank Dr. Prasanta Kumar Nayak for teaching me research methodology which helped me throughout the duration of my PhD and also in thesis formatting.

I am obliged and also thankful to Dr. Sanjeev Kumar Mahto, Coordinator, School of Biomedical Engineering, IIT (BHU), Varanasi for allowing me to use the facilities required to complete my research work. I would also like to thanks Prof. Santwana Mukhopadhyay and Dr. Sanjay Kumar Rai for giving the valuable ideas or suggestions to improve my research work. I would like to thank Research Progress and Evaluation Committee (RPEC) and Department Postgraduate Committee (DPGC) members for evaluation of my research work.

I am immensely thankful to all respected faculty members Prof. Neeraj Sharma, Dr. Pradip Paik, Dr. Sanjeev Kumar Mahto, Dr. A. R. Jac Fredo, Dr. Sudip Mukherjee, Dr. Deepesh Kumar, Dr. Brijesh Kumar and Dr. Gowri Balachander for their co-operation & support during my research work.

Ministry of Education, New Delhi is gratefully acknowledged for providing fellowship during the tenure of my research work. I would like to thank Council of Scientific & Industrial Research (CSIR) and Department of Biotechnology (DBT) for awarding me International travel grant to present my research in FENS-FORUM 2022, Paris, France. I would like to express my gratitude to Neuromatch Academy for awarding me teaching assistantship for Computational Neuroscience Summer School.

I would like to thank our co-author (Mr. Pratik Purohit), senior (Ms. Bindu Kumari), juniors (Mr. Mahatim Singh, Mr. Brijesh Baghel), and batchmates (Mr. Himanshu Verma, Mr. Aquib Siddiqui, Ms. Poorvi, Mr. Vishal, Mr. Bharat Sahu, Dr. Vikas, Ms. Shreyasi Majumdar, Ms. Prachi Srivastava, Ms. Rinki Verma, Mr. Vivek Verma) for all the moral, social, and technical support during my research work.

I would also like to deliver my warm thanks to all the supporting nonteaching staff of the department specially Mr. Bhuwaneshwari Sharan, Dr. Anuj Srivastava, Mr. Avinash Kumar Srivastava, Mr. Bharat Kumar Vishwakarma, Mr. Divyanshu Singh, Mr. Kishori Lal, Mr. Varun Kumar Pandey, and Mr. Ajay Kumar for their technical assistance and cooperation throughout my dissertation work. Without their invaluable support I was unable to fulfill my work properly.

I would like to thank my students from "Gyaan Udyaan", a group that focuses on the education and sanitation of underprivileged children on the IIT(BHU), Varanasi campus, for their constant encouragement to continue my research so that I can make greater contributions to society.

Last but not least, the profundity of one's emotions cannot be expressed with words. I would like to express my deepest gratitude to my parents, brother, sister, and sister-in-law, whose unwavering love, moral support, and blessings have inspired me to succeed in my studies, allowing me to reach this pinnacle in the journey of existence. I take great privilege to express my heartfelt thanks to all those who have directly or indirectly helped me getting through this research work successfully.

Date: 27<sup>th</sup> July, 2023  
Place: IIT (BHU), Varanasi

*Anindita Bhattacharjee*  
Anindita Bhattacharjee

## List of Figures

**Figure 1:** Computational approaches used in drug repurposing: Different computational methods can be used alone or together to analyze different types of large-scale data in a structured way to get valuable insights for repurposing theories.

**Figure 2:** Depiction of evidence of A $\beta$  undergoing enterohepatic circulation.

**Figure 3:** Depiction of the mechanism of action of the receptors to promote the A $\beta$  clearance from the body as well as the therapeutic agents that may be used to increase the expression of those receptors.

**Figure 4:** Computed structural and binding features of the a) ATP-binding cassette super family G member 2 (ABCG2), b) Multidrug Resistance Protein 1 (MDR1), c) Liver X Receptor beta (LXR-beta), d) Apical sodium bile transporter (ASBT) and e) Bile salt export pump (e) with 42-residue human A $\beta$  respectively. Human ABCG2 (PDBid: 6FEQ) in grey, MDR1 (PDB id: 2CBZ) in yellow, LXR-beta (PDB id: 1PQ6) in green, ASBT (PDB id: 3ZUX) in cyan, BSEP (PDB id: 6LR0) and A $\beta$  (PDB id: 2 MXU) in pink color downloaded from PDB and used for the present study (Visualization using UCSF Chimera).

**Figure 5:** Structural details at the interface between a) ABCG2, b) MDR1, c) LXR-beta, d) ASBT, e) BSEP and A $\beta$ . Structural figures were made using PyMOL (the PyMOL Molecular Graphics System, v.2.0 Schrodinger).

**Figure 6:** Computed structural comparison and binding features (visualization using UCSF Chimera and AutoDock) of drugs rifampicin, 24-hydroxycholesterol, resveratrol, and cilostazol against PXR (PDB id: 1SKX), b) LXR-beta (PDB id: 1PQ6), c) ASBT (PDB id: 3ZUX), and d) Phosphodiesterase 3B (PDB id: 1SO2), respectively

**Figure 7:** (a) The root mean square deviation (RMSD); (b) The root mean square fluctuation (RMSF); and (c) graphs of ligand properties for the rifampicin during 50 ns simulation runs on PXR (pregnane X receptor).

**Figure 8:** (a) The root mean square deviation (RMSD); (b) The root mean square fluctuation (RMSF); and (c) Ligand properties graph for the 24-hydroxycholesterol during 50 ns simulation runs on LXR- $\beta$  (liver X receptor).

**Figure 9:** (a) The root mean square deviation (RMSD); (b) The root mean square fluctuation (RMSF); and (c) Ligand properties graph for the resveratrol during 50 ns simulation runs on ASBT (Apical Sodium-Dependent Bile Acid Transporter).

**Figure 10:** (a) The root mean square deviation (RMSD); (b) The root mean square fluctuation (RMSF); and (c) Ligand properties graph for the cilostazol during 50 ns simulation runs on PDE3 (Phosphodiesterase-3).

**Figure 11:** (a) Stacked bar chart representation of rifampicin with active site amino acid residues of PXR (pregnane X receptor); (b) Ligand-protein contacts of rifampicin-PXR complex, and (c) Timeline representation for 50 ns simulation run analysis of rifampicin and PXR docked complex.

**Figure 12:** a) Stacked bar chart representation of 24-hydroxycholesterol with active site amino acid residues of LXR- $\beta$  (liver X receptor); b) ligand-protein contacts of 24-hydroxycholesterol-LXR- $\beta$  complex and c) timeline representation for 50 ns simulation run analysis of 24-hydroxycholesterol and LXR- $\beta$  docked complex.

**Figure 13:** a) Stacked bar chart representation of resveratrol with active site amino acid residues of ASBT (Apical Sodium-Dependent Bile Acid Transporter); b) ligand-protein contacts of resveratrol-ASBT complex and c) timeline representation for 50 ns simulation run analysis of resveratrol and ASBT docked complex.

**Figure 14:** a) Stacked bar chart representation of cilostazol with active site amino acid residues of PDE3 (Phosphodiesterase-3); b) ligand-protein contacts of cilostazol -PDE3 complex and c) timeline representation for 50 ns simulation run analysis of cilostazol and PDE3 docked complex.

**Figure 15:** The GEO2R analysis showed that LXR agonist and PXR agonist upregulates expression of a) ABCA1, b) SCD, and c) ABCB1 genes.

**Figure 16:** Protein-protein interaction networks (PPIs) of DEGs were constructed using STRING database, upregulated genes for a) GSE124053 profile of LXR- $\beta$ , and b) GSE55746 profile of PXR

**Figure 17:** Gene ontology analysis was performed for functional analysis of DEGs by using ClueGo app from Cytoscape. This app allows simultaneous analysis of multiple annotation and ontology sources. Functionally grouped network is represented, a) upregulated genes for GSE124053 dataset and b) upregulated genes for GSE55746 dataset. The node size represents enrichment significance and connections are based on kappa score ( $> 0.4$ ). In upregulated gene group for GSE124053 profile shows maximum number of nodes which are in green color represent the sterol and triglyceride metabolic process and GSE55746 profile shows cell cycle process (brown nodes), detoxification (pink nodes) and collagen related (blue nodes)

**Figure 18:** Genes with the greatest changes in expression. We observed that the top ranked hub genes in PPI network which were upregulated were associated with a) cholesterol efflux and b) cell cycle regulator.

**Figure 19:** Sub-network analysis was conducted by using the Molecular Complex Detection (MCODE) app from Cytoscape. Top sub-networks on the basis of MCODE score (Degree cut-off = 2, node score cut-off = 0.2, k-core = 2 and max. depth = 100). Upregulated gene group clusters, we identified seed nodes (ACSS2 and Mcm6) for GSE124053 profile of LXR and GSE55746 profile of PXR (highlighted in yellow) respectively.

**Figure 20:** Connectivity Map of the relationships of the drug molecules with receptors, and intermediary molecules are interconnected between themselves to simulate reciprocal relationships (upstream and downstream).

**Figure 21:** Synergy score a) Zero Interaction Potency (ZIP) and b) Bliss for drug combinations.

**Figure 22:** From left to right, dose-response, ZIP, Bliss synergy metrics in contour plot format were generated using the SynergyFinder web tool. The darker redcolor represents high synergy for each drug concentration in the combination. Synergy is presented for a combination of cilostazol with rifampicin (a), metforminwith rifampicin (highest synergy) (b), resveratrol with rifampicin (c), metformin with cilostazol (d), resveratrol with cilostazol (e), and resveratrol with metformin. Data are represented as the mean of samples.

**Figure 23:** Schematic representation of the outcome of this study, underscoring that AD can be taken to be as orchestration of multi-organ pathophysiology, namely that of the brain, liver, vascular system, and alimentary tract.

**Figure 24:** Image analysis methodology (amyloid PET scanning evaluation).

**Figure 25:** Serum cholic acid level in Alzheimer's disease is less than half of normal subjects (statistical significance is substantial, with  $p = 0.0053$ ).

**Figure 26:** Whole brain and region-wise cerebral blood flow (a), amyloid-load (b), and mini-mental state examination score (c), in normal individuals and Alzheimer's disease subjects. The statistical significance measure  $p < 0.05$  when Alzheimer's disease group is compared with cognitively normal group for each of the nine figure panels.

**Figure 27:** Differences in amyloid load (SUVR) displayed for PET images after correcting for partial volume effects (PVC). The figures are presented as SUVR colorscale; the value of amyloid deposition increases along the colour spectrum continuum: blue-yellow-red.

**Figure 28:** Correlation between mini-mental state examination (MMSE) score with amyloid load (a), and with cerebral blood flow (b). There is negative correlation between amyloid load and MMSE (a), but positive correlation between cerebral blood flow and MMSE. All interactions were statistically significant ( $p < 0.05$  in both cases).

**Figure 29:** Receiver-Operating Curves for amyloid load SUVR (a), cerebral blood flow CBF (b), and the Areas under the ROC curve (c) in the whole brain and ROIs (hippocampus, precuneus and posterior cingulate cortex) of normal individuals and Alzheimer's subjects. The sensitivity and specificity are calculated using Youden's J statistic for the ROC curves. In the vertical axis of panel (c), the value of area closes to 1 represents highest discrimination power of the parameter and lower values of area suggests less discrimination power, and indicates that the corresponding ROC curve in (a) or (b) is close to the diagonal line of identity at which there is possibility of least discrimination between healthy and diseased subjects.

**Figure 30:** Scatterplots of the interaction between serum cholic acid concentration with amyloid load (SUVR) and cerebral blood flow (CBF). All values are represented in z-scores and the interactions were statistically significant ( $p < 0.05$ ).

**Figure 31:** Animal Experimentation-based mechanistic validation of the mathematically-predicted causation relationship: Cholic acid inhibits Amyloid beta formation. The biochemical pathways are obtained from the rodent investigations.

**Figure 32:** Preclinical experimental corroboration of the predicted causality linkage: increasing amyloid beta inhibits cerebral blood flow. The biophysical changes shown in the figure are observed in the animal studies.

**Figure 33:** Relationship of mini-mental state examination MMSE score with amyloid-beta load SUVR (a), and with cerebral blood flow CBF (b) in normal subjects, showing the best-fit (solid) regression line, with 95% CI (dotted) in all subjects (n=50). There was no correlation of MMSE with amyloid-beta load or with CBF in normal subjects (MMSE vs SUVR:  $r^2 = 0.004072$ ,  $p = 0.6598$ ; MMSE vs. CBF:  $r^2 = 0.005026$ ,  $p = 0.6247$ ).

**Figure 34:** Relationship between amyloid-beta load and cerebral blood flow in normal subjects: (a) Whole brain, (b) Hippocampus, (c) Precuneus, and (d) Posterior cingulate cortex (PCC), showing best-fit (solid) regression line and 95% confidence interval CI (dotted) in all subjects (n = 50). There was no correlation between amyloid-beta load and cerebral blood flow in any of the panels (Whole brain:  $R^2 = 0.04796$ ,  $p = 0.1265$ ; Hippocampus:  $R^2 = 0.00004149$ ,  $p = 0.9646$ ; Precuneus:  $R^2 = 0.02014$ ,  $p = 0.3256$ ; Posterior cingulate cortex:  $R^2 = 0.007070$ ,  $p = 0.5615$ ).

**Figure 35:** Schema of the three pathways of the hepato-biliary-faecal elimination route of amyloid beta of brain, each pathway can be enhanced by a corresponding pharmacological agent.

**Figure 36:** (a) Imaging analysis procedure for diffusion tensor imaging (b) Tractography and identification of the fibres in the three segments of the brain.

**Figure 37:** Geometric motif of the white matter tract profile providing the neural fibre scaffold for amyloid migration circumferentially across the cerebrum, with the three schematic segments shown. The amyloid deposition starts at entorhinal-uncinate region E and migrates bidirectionally as segment-1 and then circles across the cerebrum, by segments 2 and 3.

**Figure 38:** (a) Amyloid distribution stages as Alzheimer's disease progresses over time, as observed by microscopic histopathological examination of amyloid plaques denoted by red markings. Braak Stage- A begins with initial amyloid deposits in the isocortex, as the basal zones in frontal and temporal regions. Stage-B shows amyloid gradual spread into ventral two-thirds portion of the frontal, occipital and parietal regions, including the isocortical association areas, except the superior cerebral portion as the sensory and motor regions in the dorsal vertex. Stage-C is late-stage situation where amyloid spreads throughout the cerebral isocortex, including primary sensory and motor region in the cerebral dorsal vertex. (b): The corresponding nerve fasciculus that may act as scaffolds for the amyloid migration, the fasciculus being demarcated by DTI tracking.

**Figure 39:** Neural tract impairment in AD patients at Segment-1 (orbitofrontal and uncinata region): Increase of diffusivity indices in AD subjects over controls: (a) Mean

Diffusivity, (b) Axial Diffusivity, and (c) Radial Diffusivity. The p-value is highly significant and there is large effect size.

**Figure 40:** Dysfunctionality of Neural tract in AD patients at Segment-3 (cingulate and parietal association region): The panels show that diffusivity indices accentuate in AD subjects over controls: (a) Mean Diffusivity, (b) Axial Diffusivity, and (c) Radial Diffusivity. The rise is of high statistical significance ( $p \leq 0.005$ ). It may be remarked that the p-value is highly significant, together with large effect size.

**Figure 41:** AD patients show dysfunctionality of fibre tracts at Segment-2 (parietal and inferior frontal regions). There is rise of diffusivity indices in AD subjects over controls: (a) Mean Diffusivity, (b) Axial Diffusivity, and (c) Radial Diffusivity. There is high significance in p-value, with the effect size being large.

**Figure 42:** Intensity of downregulation of the genes ABCB11, ABCA1 and MDR1 respectively in segment 1 (frontal sector), segment 2 (temporal-occipital sector) and segment 3 (parietal-dorsal sector).

**Figure 43:** Physiological routes, receptors and pharmacomodulation of hepatic clearance of amyloid from different brain regions.

**Figure 44:** Cell signaling pathways during mild and severe infections with SARS-COV2 and proposed therapeutic intervention of phytochemicals, tetracycline and cephalosporin ligands. (1) Mild infection with SARS-COV2, mainly lungs get affected, causing a high number of cytolytic T cells in the lungs. Phytochemicals act by targeting the T cells and monocytes, driving the cytokine storm in patients, leading to neuroinflammation. (2) Severe infection with SARS-COV2, affecting both lungs and the brain. Virus transmitting through a gustatory and olfactory nerve (tractography)-mediated route, causing neuroinflammation alleviated by Minocycline. Docking studies of phytochemicals, tetracycline and cephalosporin ligands, with the SARS-COV2 spike receptor-binding domain and main protease verify our approach.

**Figure 45:** The quantitative model of drug interaction with a viral receptor based on its potency

**Figure 46:** Diffusion MRI fiber tracking-connecting pons with the gustatory nerves. (A) pons to cranial nerves VII, (B) pons to cranial nerves IX, (C) pons to cranial nerves X, and (D) pons to cranial nerves XII.

**Figure 47:** Diffusion MRI fiber tracking connecting medulla oblongata with gustatory nerves. (A) medulla to cranial nerve VII, (B) medulla to cranial nerve IX, (C) medulla to cranial nerve X, and (D) medulla to cranial nerve XI.

**Figure 48:** Diffusion MRI fiber tracking connecting the olfactory nerve with (A) the hippocampus, (B) the entorhinal cortex, and (C) the amygdale.

**Figure 49:** The binding site of ACE inhibitors and SARS-COV2 spike protein.

**Figure 50:** Computed structural comparison, binding features, and the 2D interaction plot (visualization using UCSF Chimera, AutoDock and Biovia discovery studio) of MLN-4760 ((S,S)-2-{1-carboxy-2-[3-(3,5-dichlorobenzyl)-3H-imidazol4-yl]-ethylamino-4-methylpentanoic acid) (A) and lisinopril (B), with two binding sites of the ACE-2 receptor (PDB ID: 1R4L and 6M0J, respectively).

**Figure 51:** Interacting amino acid residues between the Angiotensin-Converting Enzyme 2 (ACE2) receptor and SARS-COV2 Receptor Binding Domain (RBD) (A) and the 2D interaction plot (B), visualized using PyMol and LigPlus.

**Figure 52:** Computed structural comparison and binding features (visualization using UCSF Chimera and AutoDock) of Chlorogenic acid (A), Ervacycline (B), Rolitetracycline (C), Tigecycline (D), Minocycline (E), and Naringenin (F) with Angiotensin-Converting Enzyme Receptor 2.

**Figure 53:** Computed structural comparison and binding features (visualization using UCSF Chimera and AutoDock) of Chlorogenic acid (A), Tigecycline (B), Podophyllotoxin (C), Ervacycline (D), Quercetin (E), and Minocycline (F), with SARS-COV2 main protease. The lower the binding energy, the greater will be the binding affinity.

**Figure 54:** Computed structural comparison and binding features (visualization using UCSF Chimera and AutoDock) of Ervacycline (A), Tigecycline (B), Chlorogenic acid (C), and Minocycline (D), with NS3 helicase/nucleoside triphosphatase of Japanese encephalitis.

**Figure 55:** The simulated mathematical model of drug activities toward receptors based on the clinical trial study.

**Figure 56:** GeneMANIA networks showing the gene-gene interaction results of Quercetin targets. Network displays the strength of interaction (edge thickness), type of interaction (colors), many edges in between nodes, and the score (size of node).

**Figure 57:** GeneMANIA networks showing the gene-gene interaction results of Ceftriaxone targets. Network displays the strength of interaction (edge thickness), type of interaction (colors), many edges in between nodes, and score (size of node).

**Figure 58:** GeneMANIA networks showing the gene-gene interaction results of Minocycline targets. Network displays the strength of interaction (edge thickness), type of interaction (colors), many edges in between nodes, and score (size of node).

**Figure 59:** GeneMANIA networks showing the gene-gene interaction results of Chlorogenic acid targets. Network displays the strength of interaction (edge thickness), type of interaction (colors), many edges in between nodes, and score (size of node).

**Figure 60:** GeneMANIA networks showing the gene-gene interaction results of Naringenin targets. Network displays the strength of interaction (edge thickness), type of interaction (colors), many edges in between nodes, and score (size of node).

**Figure 61:** GeneMANIA networks showing the gene-gene interaction results of Podophyllotoxintargets. Network displays the strength of interaction (edge thickness), type of interaction (colors), many edges in between nodes, and score (size of node).

**Figure 62:** The KEGG pathway of Coronavirus Disease. The critical genes identified with CytoNCA are highlighted, and their role in cytokine storm-mediated neuroinflammation is depicted



## List of Tables

**Table 1.** The binding energy, inhibitory constant (K<sub>i</sub>) value and interacting amino acid residues of drugs rifampicin, 24-hydroxycholesterol, resveratrol, cilostazol and metformin against PXR (PDB id: 1SKX), LXR- $\beta$  (PDB id: 1PQ6), ASBT (PDB id: 3ZUX), Phosphodiesterase 3B (PDB id: 1SO2), and bile salt export pump (PDB id:6LR0) respectively.

**Table 2.** Functions of top ranked hub genes.

**Table 3.** Clinical trial data for individual proposed repurposed drugs.

**Table 4.** Amyloid- $\beta$  and Cerebral blood flow interactions in Disease-prone regions of brain in Alzheimer's patients.

**Table 5.** F-test results for "Amyloid load causatively alters cholic acid" and "Cholic acid causatively alters amyloid load".

**Table 6.** F-test results for "Cerebral blood flow causatively alters Amyloid load" and "Amyloid load causatively flow alters Cerebral blood".

**Table 7.** Summary of trials regarding cholic acid and cholate modulator derivatives.

**Table 8.** Synopsis of our systems biology approach and of collateral clinical trials for pharmacologically enhanced hepatic clearance of amyloid-beta in Alzheimer's disease

**Table 9.** Differential gene signatures of the corresponding three neuroanatomical segments that are progressively affected in AD as amyloid spreads in brain (Braak stages A-B-C). Also shown are the respective pharmacological agents and receptors involved in vascular-hepatic elimination of amyloid from those respective segments.

**Table 10.** Biological subtypes of AD and corresponding possible anatomically-based personalized pharmacological enhancement of amyloid elimination.

**Table 11.** The comparison of binding energy and inhibitory constant (K<sub>i</sub>) value of ACE inhibitors against inhibitor bound human angiotensin converting enzyme-related carboxypeptidase (ACE2) (PDB ID: 1R4L) and SARS-CoV-2 spike receptor-binding domain bound to the ACE2 receptor (PDB ID: 6M0J).

**Table 12.** The increasing order of binding energy and inhibitory constant (K<sub>i</sub>) value of phytochemicals, tetracycline class of antibiotics and ceftriaxone against with SARS-CoV-2 spike receptor-binding domain bound to the ACE2 receptor (PDB ID: 6M0J).

**Table 13.** The increasing order of binding energy and inhibitory constant (K<sub>i</sub>) value of phytochemicals, tetracycline class of antibiotics and cephalosporin against COVID-19 main protease (6LU7).

**Table 14.** The increasing order of binding energy and inhibitory constant ( $K_i$ ) value of phytochemicals, tetracycline class of antibiotics and cephalosporin against N.S. helicase/nucleoside triphosphatase of Japanese encephalitis (PDB ID: 2Z83).

**Table 15:** Total number of retrieved targets from different databases.

## List of abbreviations

---

<b>Abbreviation</b>	<b>Full Form</b>
<b>ABCG2</b>	ATP-binding cassette superfamily G member 2
<b>ABCA1</b>	ATP-binding cassette transporter A1
<b>ASBT</b>	Apical Sodium-Dependent Bile Acid Transporter
<b>ABCB11</b>	ATP-binding cassette, sub-family B member 11
<b>A<math>\beta</math></b>	Amyloid Beta
<b>ACE2</b>	Angiotensin Converting Enzyme 2
<b>AD</b>	Alzheimer's Disease
<b>ASL</b>	Arterial Spin Labeling
<b>BAs</b>	Bile Acids
<b>BSEP</b>	Bile Salt Export Pump
<b>COVID19</b>	Coronavirus disease 2019
<b>CA</b>	Cholic Acid
<b>CBF</b>	Cerebral Blood Flow
<b>CREB</b>	cAMP response element-binding
<b>DTI</b>	Diffusion Tensor Imaging
<b>EHC</b>	Enterohepatic Circulation
<b>GO</b>	Gene Ontology
<b>FDA</b>	Food And Drug Administration
<b>IPA</b>	Ingenuity Pathway Analysis
<b>JE</b>	Japanese Encephalitis
<b>KEGG</b>	Kyoto Encyclopedia of Genes and Genomes
<b>LXR-<math>\beta</math></b>	Liver-X-Receptor- $\beta$
<b>MCI</b>	Mild Cognitive Impairment
<b>MDR1</b>	Multidrug Resistance Protein 1
<b>MD</b>	Molecular dynamics
<b>MCODE</b>	Molecular Complex Detection
<b>MAP</b>	Molecule Activity Predictor
<b>MRI</b>	Magnetic Resonance Imaging
<b>PET</b>	Positron Emission Tomography
<b>PXR</b>	Pregnane X Receptor
<b>PDE3</b>	Phosphodiesterase-3
<b>PCN</b>	Pregnenolone-16-Alpha-Carbinonitrile
<b>PPI</b>	Protein-Protein Interaction
<b>RMSD</b>	Root Mean Square Deviation
<b>RMSF</b>	Root Mean Square Fluctuation
<b>Rg</b>	Radius of Gyration
<b>SASA</b>	Solvent-Accessible Surface Area
<b>SARS-COV2</b>	Severe acute respiratory syndrome coronavirus 2
<b>SCD</b>	Stearoyl-Coa-Desaturase
<b>TDP-43</b>	Transactive Response DNA Binding Protein-43
<b>QKB</b>	QIAGEN Knowledge Base
<b>ZIP</b>	Zero interaction potency

---

